RSC Advances

PAPER

View Article Online
View Journal | View Issue

Cite this: *RSC Adv.*, 2026, **16**, 24704

Synthesis and characterization of a g-C_3N_4/UiO-66/Ag_2CrO_4 ternary nanocomposite for the photocatalytic degradation of methyl orange under visible-light irradiation

Gudisa Hailu Chala, *[a] Habtamu Tegegne Metikie,[a] Ephriem Tadesse Mengesha [b] and Abi M Tadesse [c]

In this study, novel g-C_3N_4/UiO-66/Ag_2CrO_4 ternary nanocomposites with different mass ratios of Ag_2CrO_4 were synthesized effectively *via* the precipitation method for the treatment of polluted water. Solvothermal and co-precipitation techniques were used to synthesize the UiO-66 and Ag_2CrO_4 nanoparticles, respectively. The precipitation process was also used to produce binary nanocomposites (g-C_3N_4/UiO-66 and UiO-66/Ag_2CrO_4). UV-visible spectrophotometry, photoluminescence (PL) study, Fourier transform infrared (FTIR) spectroscopy, and scanning electron microscopy (SEM) evidenced ample and efficient interactions between the components within the composites. The photocatalytic activities of each nanocomposite were evaluated using aqueous solutions of model methyl orange (MO) and a real sewage sample solution collected from Hawasa Textile Industry. The photocatalytic efficiencies of the ternary nanocomposites (g-C_3N_4/UiO-66/Ag_2CrO_4, 10%, 20%, and 30% of Ag_2CrO_4) were found to be higher than those of single and binary nanocomposites due to synergistic effects in the composite, which favored efficient interfacial charge transfer and improved separation of photoinduced electron–hole pairs. In particular, the ternary nanocomposite containing 20% of Ag_2CrO_4 exhibited the highest photocatalytic activity. The effect of various experimental parameters, such as pH, initial dye concentration, photocatalyst load and scavengers' effects, on MO degradation was investigated using this g-C_3N_4/UiO-66/Ag_2CrO_4 ternary nanocomposite. Results showed that at optimum pH (2), catalyst load (0.2 g L^{-1}) and initial dye concentration (10 ppm), the percent degradation of MO under visible-light irradiation (indoor system) was found to be 97.0% in 120 min, and in the outdoor system, it was found to be 99.6% in 40 min. The selected photocatalyst was also applied for the degradation of a real sewage sample solution, and a percent degradation of 76.2% was observed. Importantly, the catalytic efficiency did not decrease significantly even after three reaction cycles, showing it had good stability and recyclability. Hydroxide radicals (*OH) and holes (h^+) were identified as the most active species in the photocatalytic process. Therefore, the g-C_3N_4/UiO-66/Ag_2CrO_4 ternary nanocomposite may be a viable option for industrial photocatalytic applications, particularly in the removal of organic dyes from wastewater.

Received 27th August 2025
Accepted 6th April 2026

DOI: 10.1039/d5ra06399j

rsc.li/rsc-advances

1. Introduction

Recently, there has been a lot of interest in metal–organic frameworks (MOFs) for photocatalysis applications.[1] Metal–organic frameworks (MOFs) are an interesting type of porous crystalline materials made of metal ions and polyfunctional organic ligands. They have attracted a lot of interest from academics in recent years because of their numerous attractive applications in drug delivery, gas storage, catalysis, and selective adsorption and separation. MOFs are promising photocatalysts because they behave like semiconductors when exposed to light.[2] In one of the ground-breaking studies, MOF-5 was investigated for the photocatalytic degradation of phenol in an aqueous solution.[3] However, due to the wide bandgap of these MOFs, the degradation process could only proceed when exposed to UV radiation. Among the different kinds of MOFs, UiO-66, a MOF based on zirconium, in several types of MOFs, UiO-66, an MOF based on zirconium, has been gaining increasing interest from researchers.[4] Stability can be preserved even after addressing missing linker defects and altering the active functional groups.[5] However, MOFs utilized as catalysts

[a]*Department of Applied Chemistry, School of Applied Natural Science, Dire Dawa University, P O Box 1362, Dire Dawa, Ethiopia. E-mail: gudisahailu0@gmail.com; habtamutegegne9@gmail.com; Tel: +251 921705490; +251 939618589*

[b]*CEA, LiDYL, Gif Sur Yvette, Ile de France, 91191, France. E-mail: eph121983@gmail.com; Tel: +33-1 69 08 81 21*

[c]*Haramaya University, Chemistry College of Natural and Computational Sciences, Dire Dawa, Ethiopia. E-mail: abi92003@yahoo.com*

in photocatalysis are not as effective as inorganic semiconductors due to their low efficiency for solar energy conversion and photo-generated charge separation.[6] To solve this serious problem, additional semiconductor functional materials with photocatalytic activities can be installed on MOF substrates to increase stability and catalytic activity. UiO-66 is usually mixed with other semiconductors with narrow bandgaps to modify the energy levels of the valence band, conduction band, or both in the composites.

Therefore, by reducing electron–hole pair recombinations, charging injection from other semiconductors into UiO-66 can produce longer and more effective charge separation than the parent materials.[7] For example, g-C_3N_4 is an effective adsorbent and catalyst when combined with UiO-66 because it improves its accessible surface area and forms a heterojunction contact between the two components. The ultra-high porosity and exceptionally high internal surface area structure of MOFs are preserved in UiO-66/g-C_3N_4, potentially resolving the low-specific-surface-area problem of g-C_3N_4. Furthermore, the heterojunction between two semiconductors can reduce electron and hole recombination by facilitating electron transport and separation.

Furthermore, UiO-66/g-C_3N_4 can utilize visible light because of the low bandgap of g-C_3N_4.[8] The photocatalytic activity of g-C_3N_4/UiO-66 binary composites has been documented thus far in comparison to that of UiO-66.[8] Additionally, there are reports on ternary nanocomposites, such as rGO/UiO-66/Ag_2CO_3,[9] rGO/UiO-66/Ag_3PO_4,[10] CuO/UiO-66/Ag_2CO_3,[11] and CdS/UiO-66/Ag_3PO_4,[12] for photocatalysis applications. Ternary composite systems, such as g-C_3N_4/UiO-66/Ag_2CrO_4, have good features that may lead to improved selectivity, stability, sensitivity, and photocatalytic efficiency. To the best of our knowledge, this ternary compound, g-C_3N_4/UiO-66/Ag_2CrO_4, has not yet been reported. Therefore, the goal of the current work is to create a ternary nanocomposite of the previously stated composite for use in photocatalysis.

2. Materials and methods

2.1. Materials

All of the chemicals and solvents used were analytical grade and were purchased from commercial providers. Every chemical used was of analytical grade. No additional purification was done before using the chemical reagents. g-C_3N_4 was synthesized using urea (CH_4N_2O, BDH, 98%). Zirconium oxychloride octahydrate ($ZrOCl_2 \cdot 8H_2O$, >99.5%) salt, 1,4-benzendicarboxylic acid (H_2BDC, 98%), and DMF (99% British, BDH) were utilized to create UiO-66. Ag_2CrO_4 was prepared using deionized water, K_2CrO_4 (BDH, 98%), and $AgNO_3$ (99% British, BDH). The materials were prepared and applied using hydrochloric acid (BDH, England, 37%), ethanol (absolute grade, 99%), sodium sulphate (Merck, 99%), sodium bicarbonate (India, 99.5%), sodium hydroxide (BDH, England, 98%), and sodium nitrate. For the photocatalytic test of the as-synthesized nanocomposites, model methyl orange (MO: $C_{14}H_{14}N_3NaO_3S$, Thermo Fisher Scientific, ACS reagent, 85% dye content) and polluted water containing methyl orange were used.

2.2. Synthesis procedures

2.2.1. Synthesis of Zr-UiO-66-DMF (HT). Zr-UiO-66 was prepared using a 1 : 1 molar ratio of Zr to BDC. 3.91 g (12.78 mmol) of zirconium oxychloride octahydrate ($ZrOCl_2 \cdot 8H_2O$) salt was dissolved and agitated for 30 minutes in 50 mL of DMF. The mixture was centrifuged for half an hour; afterward, 2.01 g (12.11 mmol) of benzene dicarboxylic acid was dissolved in 50 mL of DMF. The metal salt solution was then progressively combined with the linker solution for an entire day. For the entire day, the reaction was kept in the oven at 120 °C. Following a 30-minute centrifugation at 2500 rpm, the precipitate was washed three times using DMF and four times using methanol. The solids were then weighed after being allowed to dry at room temperature in the open.[13] Zr-MOF precipitated at high temperatures was identified as UiO-66-DMF (HT). It was expected to have the chemical formula $Zr_6O_4(OH)_4 \cdot [C_6H_4(CO_2)_2]_{12}$.[4]

2.2.2. Synthesis of the g-C_3N_4/UiO-66 binary nanocomposite. According to a report,[8] the binary compound, g-C_3N_4/UiO-66, was made in a single step. The g-C_3N_4 : UiO-66 molar ratio of 0.5 : 1 served as the foundation for the creation of the g-C_3N_4/UiO-66 composite. In order to prepare 0.500 g of g-C_3N_4/UiO-66 binary nanocomposite, 0.330 g of the as-synthesised UiO-66 was sonicated for 30 minutes in 25 mL of distilled water (solution 1). Another flask was used to ultrasonically disperse 0.170 g of g-C_3N_4 in 25 mL of distilled water for 30 minutes (solution 2). After that, solution[2] was gradually added to solution[1] and vigorously agitated for 12 hours. In the end, the product was collected by filtration, thoroughly cleansed four times with distilled water, and dried in an oven at 80 degrees Celsius for twelve hours.

2.2.3. Synthesis of Ag_2CrO_4/UiO-66 binary nanocomposite. Ag_2CrO_4/UiO-66 nanocomposite was made using the technique described in ref. 14. The Ag_2CrO_4/UiO-66 nanocomposite was made using the Ag : Zr molar ratio of 0.5 : 1. Usually, 9.766 mg (0.50344 mmol) of K_2CrO_4 was dissolved in 5.034 mL of deionized water to generate 0.500 g of an Ag_2CrO_4/UiO-66 composite with an Ag : Zr molar ratio of (0.5 : 1). After that, 0.33 g (0.126 mmol) of the synthesized UiO-66 was added to the K_2CrO_4 solution, and it was agitated for an hour. Separately, 10 mL of deionized water was used to dissolve 0.170 g (1.001 mmol) of $AgNO_3$. The $AgNO_3$ solutions were added dropwise to the UiO-66 mixture. The reaction mixtures were vigorously agitated for 12 hours at room temperature after a total of 15.034 mL of water was added. Ultimately, the product was collected by filtration, carefully cleaned four times with deionized water, and dried for 12 hours at 80 degrees Celsius in an oven.

2.2.4. Synthesis of g-C_3N_4/UiO-66/Ag_2CrO_4 ternary nanocomposites. The ternary heterocomposites g-C_3N_4/UiO-66/Ag_2CrO_4 with different weight ratios were synthesized by liquid-assisted solid state reactions by varying the amount of Ag_2CrO_4. The g-C_3N_4/UiO-66/Ag_2CrO_4-*x* ternary nanocomposites of different weight ratios (10 wt%, 20 wt%, and 30 wt%) of Ag_2CrO_4 to g-C_3N_4/UiO-66 were synthesized by liquid-assisted solid-state reactions as follows. The weight-ratio mass of Ag_2CrO_4 to g-

C_3N_4/UiO-66 was varied by changing the amount of Ag_2CrO_4 added during the synthesis and keeping the g-C_3N_4/UiO-66 amount constant. First, a certain amount of the as-synthesized g-C_3N_4/UiO-66 (0.85 g) nanocomposite was dispersed in 50 mL of distilled water and sonicated for 30 min. Then, $AgNO_3$ at different weight ratios of 10 wt% (87 mg or 0.514 mmol), 20 wt% (174 mg or 1.024 mmol), and 30 wt% (261.13 mg or 1.537 mmol) were added into the above solution and stirred for 2 h. After stirring, a solution of K_2CrO_4 at different weight ratios was slowly poured [10% (49.70 mg or 0.256 mmol in 5 mL of deionized water), 20% (99.94 mg or 0.512 mmol in 8 mL of deionized water), and 30% (149.00 mg or 0.768 mmol in 12 mL of deionized water)] into the above solution and stirred for 12 hours. Finally, the product was collected by filtration, carefully cleaned four times with deionized water, and dried for 12 hours at 80 degrees Celsius in an oven.

2.3. Characterization of materials

The as-synthesized samples were characterized by X-ray diffraction (Analytical X-ray source) with Cu Kα radiation (wavelength of 0.15406 nm) at a step scan rate of 0.02 (step time: 1 s; 2θ range: 5.0°–90°). Further, UV/Vis spectrophotometry (SANYO SP65, UK), PL fluorescence spectrometry (RF-5301PCSPECTROFLUOROPHOTOMETER), FTIR spectroscopy (Spectrum65, PerkinElmer) and SEM (JCM-6000plus BENCH TOP SEM, SHIMADZU Corporation, Japan) were conducted.

2.4. Determination of the point of zero charge

By adding 100 mL of 0.01 M $NaNO_3$ to each flask and adjusting to different pH ranges from 2 to 12 using 0.1 M solutions of HCl and NaOH, the pH_{PZC} of GUA2 (g-C_3N_4/UiO-66/Ag_2CrO_4-20%) was calculated. The initial pH was then measured after adding 0.2 g of the photocatalyst to each flask, moving it to a mechanical shaker, and shaking it for 60 minutes. The aforementioned solution was then equilibrated for an additional 60 minutes after 1 g of $NaNO_3$ was added. The point of zero charge, where the graph intersected the *X*-axis, was then found by measuring the final pH and plotting pH final-initial (*Y*-axis) *vs.* pH final (*X*-axis).[15]

2.5. Photocatalytic degradation studies

The Hawasa Textile Industry provided the wastewater sample, which was treated with the chosen and comparatively more effective photocatalyst. The photocatalytic activities of the as-synthesized photocatalysts were investigated for the degradation of MO in both dark and visible light. A reactor tube was filled with 0.2 g L^{-1} of the as-synthesized photocatalyst powder and 10 ppm of a 100 mL aqueous solution of MO at pH 2 in order to prepare for the methyl orange degradation. The adsorption–desorption equilibrium was reached in the catalyst and MO dye suspension after one hour in a dark setting.[16] After that, a magnetic stirrer was used to continuously mix the suspensions while they were exposed to visible light. When stirring, air or oxygen was added to the mixture as needed. Then, absorbance was measured in a 20-min time interval to monitor the MO aqueous solution decolorization. To this effect, 10 mL of suspension was withdrawn at a 20-min time interval and centrifuged at 3000 rpm for 10 min. Finally, the percentage degradation was calculated for each case using the following formula:

$$\%\ \text{degradation} = \frac{A_o - A_t}{A_o} \times 100 = \left(1 - \frac{A_t}{A_o}\right) \times 100,$$

where A_t is the dye's absorbance at time "t", and A_o is the dye's absorbance at the beginning stage. The Langmuir–Hinshelwood model was used to express the rate at which the photocatalysts degraded methyl orange. The reaction rate can be written as indicated in ref. 17 when the original dye concentration is lower:

$$\text{Rate} = \ln(C_t/C_o) = -Kt,$$

where t (min) is the reaction time, C_o is the absorbance of MO dye in solution at the beginning, C_t is the absorbance at a specific time, and K (min^{-1}) is the apparent pseudo-first-order reaction rate constant. The adsorption of dye on the catalyst surface will be assessed by dark adsorption experiments, and C_t/C_o *vs.* irradiation duration was shown for comparison.

3. Results and discussion

3.1. Powder X-ray diffraction (PXRD) analysis

Fig. 1 shows the characteristic peaks on the XRD patterns of the as-synthesized nanocomposites: UiO-66 (U), g-C_3N_4/UiO-66 (GU), UiO-66/Ag_2CrO_4 (UA), and ternary g-C_3N_4/UiO-66/Ag_2CrO_4 (GUA2). Accordingly, the diffraction peaks observed at scattering angles (2θ) of 7.30°, 25.55°, and 43.79° corresponding to (002), (20$\underline{2}$), and (33$\underline{2}$) in the lattice plane, respectively, represented the hexagonal structure of the UiO-66 particle, which is in line with the previous report.[10] The peak observed at a scattering angle (2θ) of less than 10° was characteristic of porous materials that possess abundant pores or cavities. The diffraction peak observed at scattering angles (2θ) of 10.01° and 27.89° corresponded to the (012) and (035) crystal lattice planes of the g-C_3N_4/UiO-66 composite. In particular, the intense peak observed at a scattering angle of 27.89 represented the presence of g-C_3N_4 material in the binary system. When UiO-66 and g-C_3N_4 were suitably coupled, the maximum mass ratio of g-C_3N_4 reduced the intensity of the peak seen at scattering angles (2θ) of 10.01°, 25.55°, and 43.79° of UiO-66, indicating the creation of composites. Similarly, the integration of g-C_3N_4 with UiO-66 reduced the porosity of Zr-MOF, which in turn reduced the strength of the peak seen at a scattering angle of less than 10°. Moreover, the diffraction peak observed at scattering angles (2θ) of 10.01°, 18.7°, 27.81°, 31.26°, and 32.32°, corresponding to the (110), (102), (222), (225), and (226) crystal planes, respectively, represented the structure of the UiO-66/Ag_2CrO_4 ternary nanocomposite. When UiO-66 was coupled with Ag_2CrO_4, the diffraction peak observed at a scattering angle (2θ) of 10.01° was reduced due to the formation of a composite with Ag_2CrO_3. In the case of the ternary system (g-C_3N_4/UiO-66/Ag_2CrO_4), the peak observed at scattering angles (2θ) of 26°, 31.18°, and 33°, corresponding to the (222), (225), and (226) crystal planes,

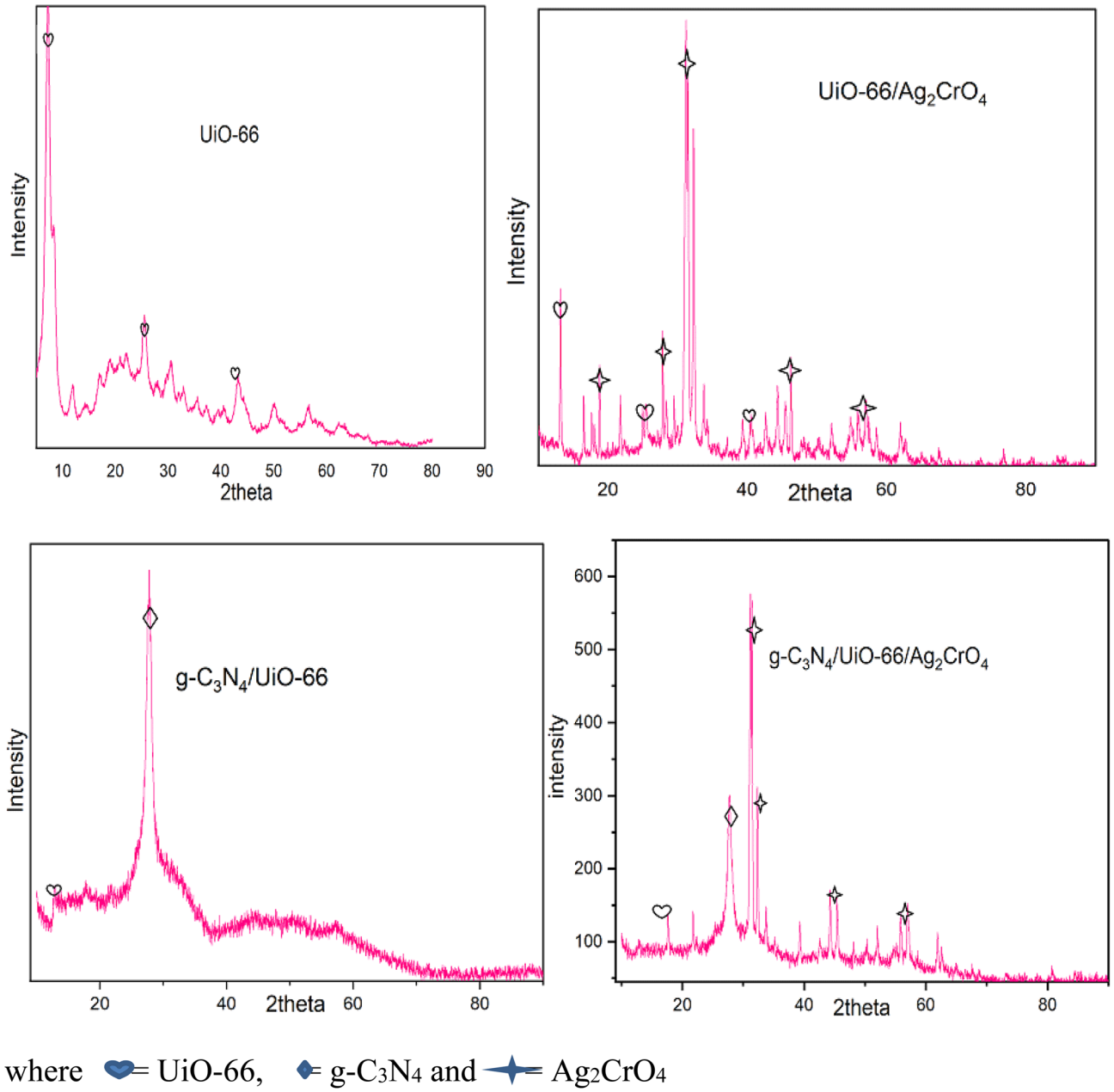

Fig. 1 XRD patterns of U, GU, UA and GUA2.

respectively, represented the formation of the ternary composite. In this instance, a new peak formed, and the detected peak at a scattering angle (2θ) of 10.01° on UiO-66 was reduced, indicating the correct incorporation of g-C_3N_4 and Ag_2CrO_4 with the host, Zr-MOF. The presence of Ag_2CrO_4 material in the ternary system was indicated by the relatively high peaks seen at scattering angles of 31.18° and 33°. The Debye–Scherer formula[18] was used to determine the average crystallite size of each of the as-synthesized material [U, GU, UA, and GUA2].

$$D = \frac{K\lambda}{\beta \cos \theta}, \quad (1)$$

where D is the crystallite size in nanometers, and K is the form factor constant, which is assumed to be 0.9. β is the full width at half maximum (FWHM) in radians, λ is the X-ray wavelength (0.15406 nm) for Cu target Kα1 radiation, and θ is the Bragg's angle. The most intense peak in the PXRD pattern was used to calculate the average crystallite size (D_s) of the as-synthesized nanocomposite. The crystallite size of the photocatalysts is one of the important factors in the photocatalytic degradation process.[18] As can be seen, the photocatalytic degradation of MO by the ternary composite increased with the decrease in the particle size. This was due to the formation of a high number of active sites on the photocatalyst surfaces, which in turn increased the number of hydroxyl and superoxide radicals.[19]

Table 1 Average crystallite sizes of the as-synthesized nanocomposites

Photocatalysts	2θ (degree)	β (radians)	D_s (nm)
U (UiO-66)	7.30	0.9259	1.500
AU (Ag_2CrO_4/UiO-66)	31.26	0.02026	7.102
GU (g-C_3N_4/UiO-66)	27.89	0.06078	2.349
GUA2 (g-C_3N_4/UiO-66/Ag_2CrO_4)	31.18	0.1418	1.013

The likelihood of an electron–hole pair recombining was reduced with the decrease in the particle size. This was due to the possibility of increasing the distance needed for charge carriers to migrate to the surface. In the presence of various supports, this type of charge movement can also be assisted. They can postpone electron–hole pair recombination even more. The average crystallite sizes (D_s) of the as-synthesize materials are described in Table 1.

3.2. UV-vis diffuse absorption spectra

Plotting absorbance against wavelength yielded the UV-Vis diffuse absorption edges of the as-synthesized photocatalysts. The value of the diffuse absorption edge (nm) was obtained by intercepting the tangent line on the descending portion of the absorption peak at the wavelength axis. The bandgap energy of each of the as-synthesized material was determined by the following formula:

$$\text{Bandgap energy(eV)} = \frac{1240}{\text{absorption edge(nm)}}. \quad (2)$$

The bandgap energy (E_g) of each of the as-synthesized photocatalyst was also obtained from the equation shown below.

$$\alpha h\nu = A(h\nu - E_g)^{n/2}. \quad (3)$$

The absorption coefficient, Planck constant, light frequency, bandgap energy, and absorption constant are represented by α,

Table 2 Bandgap energy of the as-synthesized nanomaterials[a]

Nanomaterials	Estimated bandgap energy (eV)	Absorption edge (nm)	Reported bandgap energy (eV)	References
G	2.57	480 nm	2.57	21
U	3.80	326 nm	3.84	21
A	1.90	652 nm	1.80	22
GU	3.07	404 nm	3.74	21
UA	2.48	500 nm		This work
GUA1	2.23	556 nm		This work
GUA2	2.14	580 nm		This work
GUA3	2.21	561 nm		This work

[a] where G = g-C_3N_4, A = Ag_2CrO_4, U = UiO-66, GU = g-C_3N_4/UiO-66, AU = Ag_2CrO_4/UiO-66 and GUA = g-C_3N_4/UiO-66/Ag_2CrO_4 (GUA1 = 10% of Ag_2CrO_4, GUA2 = 20% Ag_2CrO_4 and GUA3 = 30% Ag_2CrO_4).

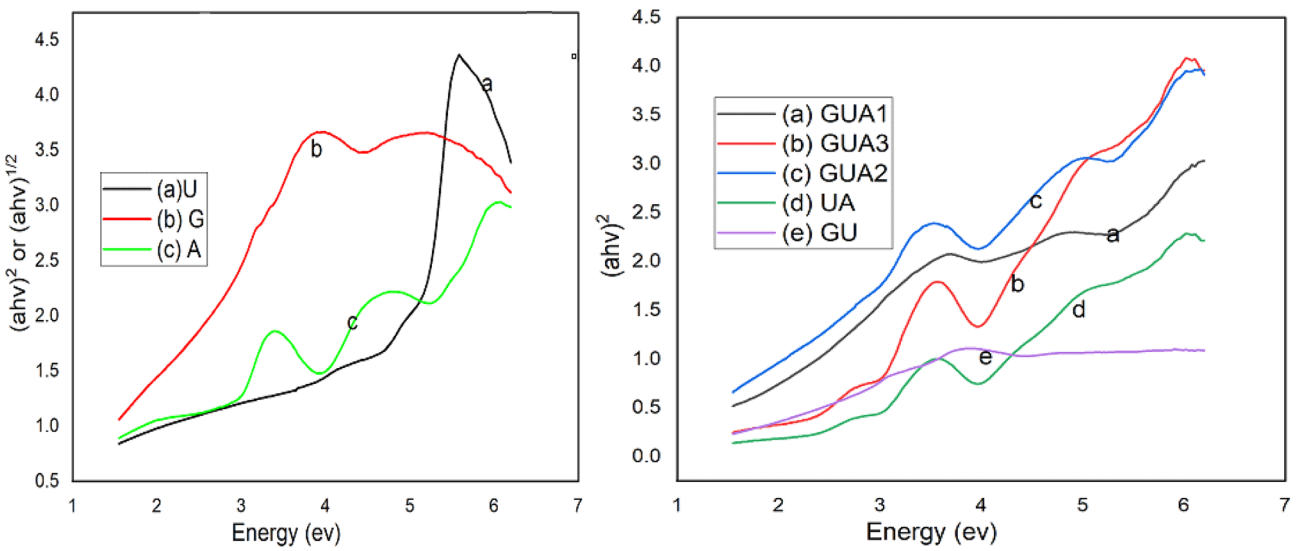

Fig. 2 (a) Plot of $(\alpha h\nu)^2$ *versus* photon energy ($h\nu$) for the as-synthesized materials: G, U, A, GU, UA, GUA1, GUA2, and GUA3. First graph: (a) U (UiO-66), (b) G (g-C_3N_4), and (c) A (Ag_2CrO_4). Second graph: (a) GUA1 (g-C_3N_4/UiO-66/Ag_2CrO_4 10%), (b) GUA3 (g-C_3N_4/UiO-66/Ag_2CrO_4 30%), (c) GUA2 (g-C_3N_4/UiO-66/Ag_2CrO_4 20%), (d) UA (UiO-66/Ag_2CrO_4), and (e) GU (g-C_3N_4/UiO-66).

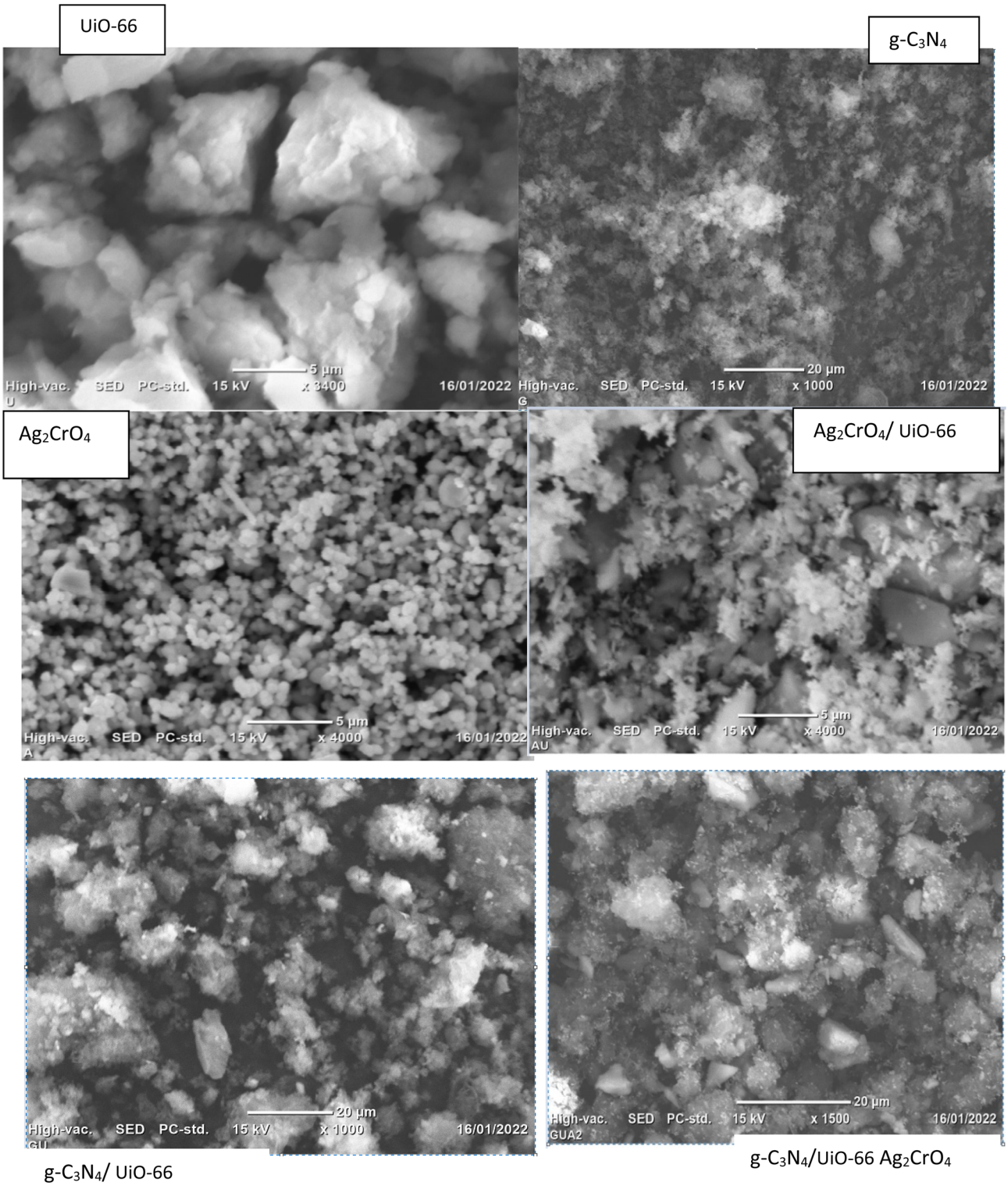

Fig. 3 SEM images of the as-synthesized photocatalysts.

h, ν, E_g, and A, respectively. The value of n was decided by the property of the semiconductor; for an indirect bandgap semiconductor, such as Ag_2CrO_4, the value of n is 4, and for a direct bandgap semiconductor, such as g-C_3N_4, the value of n is 1.[20] Based on the Tauc plot (eqn (3)), the bandgaps for all the as-synthesized materials, such as G (g-C_3N_4), U (UiO-66), A (Ag_2CrO_4), GU (g-C_3N_4/UiO-66), UA (UiO-66/Ag_2CrO_4) and ternary GUA1, GUA2 and GUA3 (g-C_3N_4/UiO-66/Ag_2CrO_4), were determined, and their photocatalytic performances towards the degradation of MO dye were decided, because bandgap energy tells the photocatalytic mechanism of the material during dye degradation. Table 2 describes the bandgap energy of each of

the as-synthesized material, which was determined by Tauc's equation. The absorption edge of Zr-MOF (UiO-66) was at 326 nm, which was outside the visible region. Hence, its photocatalytic activity towards the degradation of MO was lower than that of the other as-synthesized photocatalysts, as shown in Table 2, which is in line with the previous report.[8] However, proper coupling with g-C_3N_4 and Ag_2CrO_4 made it shift towards the visible regions, with an absorption edge of 580 nm (GUA2), as shown in Table 2 and (Fig. 2).

3.3. SEM analysis of photocatalysts

The SEM micrograph of the as-synthesized materials is depicted in Fig. 3. It could be seen from Fig. 3 that the SEM micrographs of all the single, binary and ternary systems showed no distinct morphologies. The pure Ag_2CrO_4 showed irregular and stacked particle-like morphology, which was obviously agglomerated. In the binary system, Ag_2CrO_4/UiO-66, it could be clearly observed that some irregular Ag_2CrO_4 nanoparticles were deposited on the surface of UiO-66, demonstrating that the Ag_2CrO_4 nanoparticles securely adhered to the support and progressively grew on the surface of MOFs during the solution phase reaction. Notably, in contrast to pure Ag_2CrO_4, the *in situ* growth created close contact between Ag_2CrO_4 and MOFs (UiO-66), which improved photogenerated charge carrier transfer and separation. In the case of binary g-C_3N_4/UiO-66 and ternary g-C_3N_4/UiO-66/Ag_2CrO_4 systems, no discernible morphology was observed, indicating the complete mixing up of the components upon composite formation.

3.4. FTIR study of the as-synthesized materials

The O–H stretching vibration may be responsible for UiO-66's distinctive peak at 3420 cm^{-1}. In agreement with the earlier report,[4] the distinctive peaks at 1662 cm^{-1}, 1584 cm^{-1}, and 1398 cm^{-1} were attributed to the stretching vibrations of C=O in the carboxylic acid found in H_2BDC. This band indicated the existence of a coordinate bonding of the metal with the organic fraction of terephthalic acid. This is in agreement with the previous report.[23] The peaks at 748 cm^{-1} and 663 cm^{-1} were due to the Zr-(μ_3)-O bond, which is in line with the previous reports.[4,9] The small bands at 1504 cm^{-1} and 1245 cm^{-1} represented the typical frame vibration of a benzene ring. The O–H stretching vibrations for the binary (GU) and ternary GUA2 nanocomposites were 3415 cm^{-1} and 3393 cm^{-1}, respectively. Moreover, in the case of g-C_3N_4/UiO-66 and g-C_3N_4/UiO-66/Ag_2CrO_4 ternary nanocomposites, there was a shift in the stretching vibration of the carbonyl C=O group. In contrast to UiO-66, the stretching vibration of C=O for the binary and ternary systems changed into a relatively low wave number. The interaction of UiO-66 with Ag_2CrO_4 and g-C_3N_4 materials to generate composites may be the cause of these shifts in the distinctive peaks of UiO-66 to the low wave numbers. Shifting the peaks to a low wave number benefits the photo-generated electron transfer; this enhances the photo-catalytic activities of composites. For binary (g-C_3N_4/UiO-66) and ternary (g-C_3N_4/UiO-66/Ag_2CrO_4) composites, the absorption bands centered at 3212 cm^{-1} and 3208 cm^{-1}, respectively, were attributed to the stretching vibrations of N–H bonds. Additionally, the typical

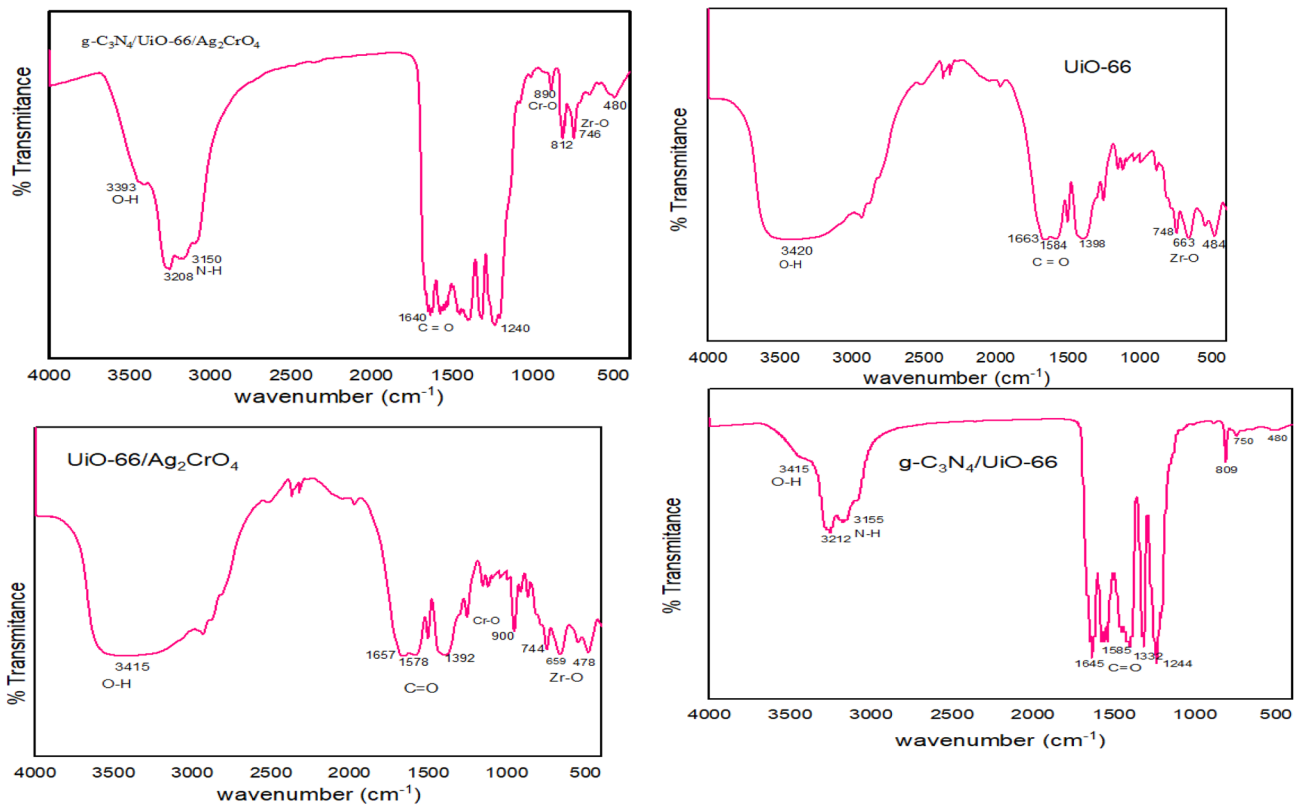

Fig. 4 FTIR spectra of the as-synthesized materials (U, GU, UA and GUA2).

skeletal stretch ring vibrations of the s-triazine or tri-*s*-triazine groups were attributed to a set of significant absorption bands in the range of 1240–1640 cm^{-1}. According to earlier findings, the steep peaks at 812 cm^{-1} are associated with the normal breathing style of triazine units.[24] The FTIR spectra of binary ($UiO\text{-}66/Ag_2CrO_4$) and ternary ($g\text{-}C_3N_4/UiO\text{-}66/Ag_2CrO_4$) nanocomposites showed a strong absorption band at 900 cm^{-1} and 890 cm^{-1}, respectively, which were assigned to the stretching vibration mode of the Cr–O bond, which is in line with the previous report (Fig. 4).[25]

3.5. Photoluminescence (PL) study of the as-synthesized photocatalysts

It could be observed that the PL intensities of the binary and ternary nanocomposites were much lower as compared to those of single UiO-66. The intensity levels were as follows: U > G > A > AU > GU > GUA1 > GUA3 > GUA2. This is, of course, in good agreement with the results observed in the photocatalytic degradation curves presented in Fig. 5. Excitonic PL intensity decreased in the binary and ternary composite systems due to the effective separation of photo-induced electrons and holes. This is due to the fact that linked materials have a strong ability to collect photo-induced electrons when the excitonic PL intensity is low. Consequently, improved charge separation between photo-generated electrons and holes results in increased photocatalytic activity. In contrast, the PL intensity of the $g\text{-}C_3N_4/UiO\text{-}66/Ag_2CrO_4$ photocatalyst dramatically dropped, indicating a substantially low rate of photo-generated electron–hole (e^-–h^+) pair recombination. Therefore, the enhancement of photocatalytic activity has a good agreement with the decrease in PL intensity.

3.6. Photocatalytic studies of the as-synthesized nanocomposites

The MO photodegradation curves *via* the as-synthesized $g\text{-}C_3N_4/UiO\text{-}66/Ag_2CrO_4$ hybrids were evaluated under visible-light irradiation at a maximum absorption (λ_{max}) of 508 nm. The binary composites, such as the $g\text{-}C_3N_4/UiO\text{-}66$ and $Ag_2CrO_4/UiO\text{-}66$ systems, showed higher degradation efficiency on MO dye under visible-light irradiation than the single photocatalyst, UiO-66, because of the retardation of the back reaction between $g\text{-}C_3N_4$ and Ag_2CrO_4 with UiO-66, which produced a great number of charge carriers that increased the degradation efficiency (Fig. 6).

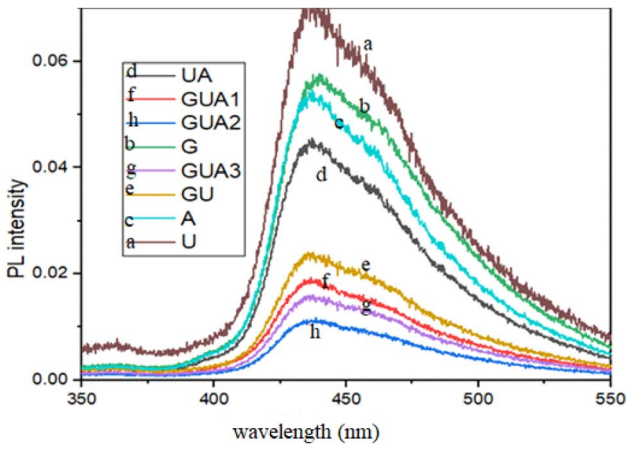

Fig. 5 Comparison of the photoluminescence (PL) spectra of the as-synthesized materials: (d) UA ($UiO\text{-}66/Ag_{22}CrO_{44}$), (f) GUA1 ($g\text{-}C_{33}N_{44}/UiO\text{-}66/Ag_{22}CrO_{44}$ 10%), (h) GUA2 ($g\text{-}C_{33}N_{44}/UiO\text{-}66/Ag_{22}CrO_{44}$ 20%), (b) G ($g\text{-}C_{33}N_{44}$), (g) GUA3 ($g\text{-}C_{33}N_{44}/UiO\text{-}66/Ag_{22}CrO_{44}$ 30%), (e) GU ($g\text{-}C_{33}N_{44}/UiO\text{-}66$), (c) A ($Ag_{22}CrO_{44}$), and (a) U (UiO-66).

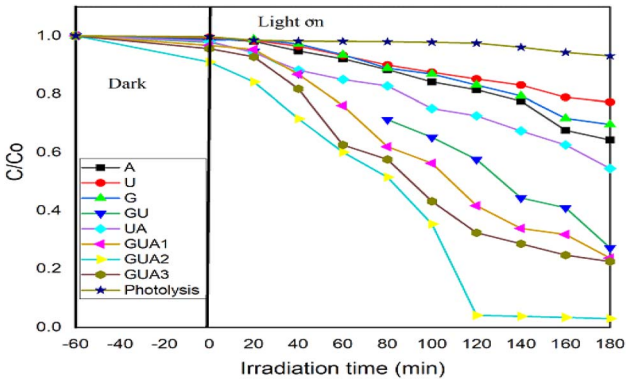

Fig. 6 Comparison of the photocatalytic activity of the as-synthesized single, binary and ternary photocatalysts at optimized parameters (at pH = 2, 10 ppm dye concentration and 0.20 g per L catalyst load) under visible-light irradiation.

3.7. Effect of experimental parameters on the degradation of MO under visible-light irradiation

3.7.1. pH of the MO aqueous solution. The pH of the MO solution was changed from pH 2.0 to pH 12.0 using 0.1 M solutions of HCl and NaOH in order to examine the impact of pH on the adsorption capacity and degradation efficiency of MO. Additionally, Fig. 7 displays the photodegradation efficiency of the MO solution, with a catalyst load of 0.15 g L^{-1} and a starting concentration of 15 ppm as a function of contact time. According to the experimental findings, the MO solution's greatest adsorption and photodegradation efficiency was discovered at pH = 2. The high adsorption capacity for MO may result from the electrostatic attraction between the positively charged $g\text{-}C_3N_4/UiO\text{-}66/Ag_2CrO_4$ (GUA2) adsorbent surface and the negatively charged anionic MO dye when the pH of the solution is less than the pH of PZC of $g\text{-}C_3N_4/UiO\text{-}66/Ag_2CrO_4$ (GUA2), which is 6.02. The decreased photodegradation efficiency of MO at a high pH may be due to a high concentration of OH-ions, which prevents the penetration of visible light. The production of hydroxyl radicals is increased at high pH values.[26] However, when the pH of the solution is excessively high (pH > 12), the breakdown of organic molecules is suppressed because hydroxyl ions compete with organic molecules for adsorption on the catalyst surface.[27] On the other hand, because the photocatalyst's surface is positively charged at a low pH, there is an increase in the adsorption of anionic organic molecules on its surface. Furthermore, the efficiency of the dye's breakdown in the photocatalytic process is determined by the quantity of photogenerated electrons and holes that reach the particle

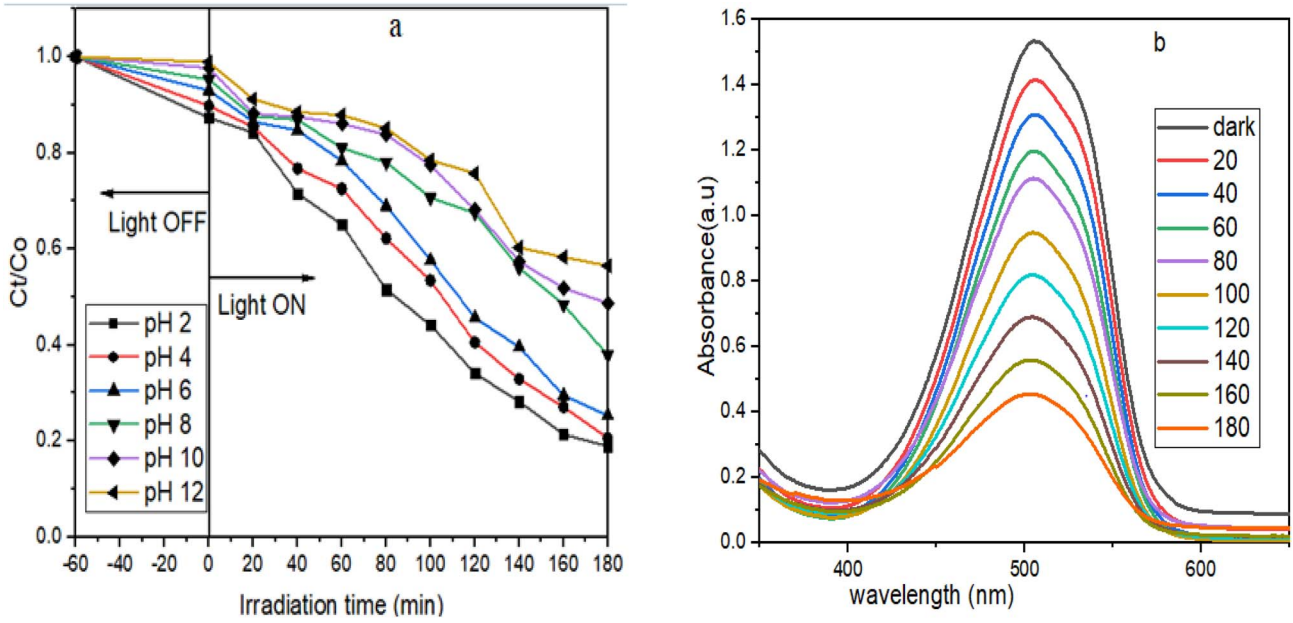

Fig. 7 (a) Effect of pH on the photocatalytic activities of the as-synthesized nanocomposite (GUA2) with respect to irradiation time, (b) UV-visible spectra of MO solution irradiated in 20-min intervals at 15 ppm dye concentration, 0.15 g per L catalyst loading and pH 2.

surface.[28] Clearly, the degradation was fastest at pH 2, 4, and 6 in acidic media and slowest at basic pH. The semiconductor particle surface was positively charged at more acidic pH values, while at pH > 6.02, the surface was negatively charged. This had important consequences for the adsorption and desorption properties of the particle surface of the catalyst, as well as for the photo-adsorption and photo-desorption features of such surfaces. Thus, an anionic dye with a negative charge can be adsorbed on the surface of a highly positively charged as-synthesized nanocomposite *via* a strong electrostatic attraction and electrostatic interaction, which was beneficial for increasing the adsorption property and thereby improving the degradation efficiencies of the material prepared at pH 2. The general trend is similar to that of a previous study done for photocatalytic degradation of methyl orange (MO) with the Ti-BDC metal–organic framework.[29]

3.7.2. Photocatalyst load. Under visible light irradiation, the impact of photocatalyst load on methyl orange photo degradation was examined. The catalyst concentration is regarded as one of the most crucial factors that should be examined in any decolorization process from an economic perspective. Finding the ideal photocatalyst load for effective dye removal is essential to preventing the usage of excess photocatalyst. Using varied concentrations of the g-C_3N_4/UiO-66/Ag_2CrO_4 catalyst, ranging from 0.10 to 0.30 g L^{-1}, while maintaining all other experimental parameters (at 15 ppm dye concentration and pH 2), the impact of catalyst amount on the photocatalytic decolorization process of MO was initially examined. The C_t/C_0 result of methyl orange dye *versus*

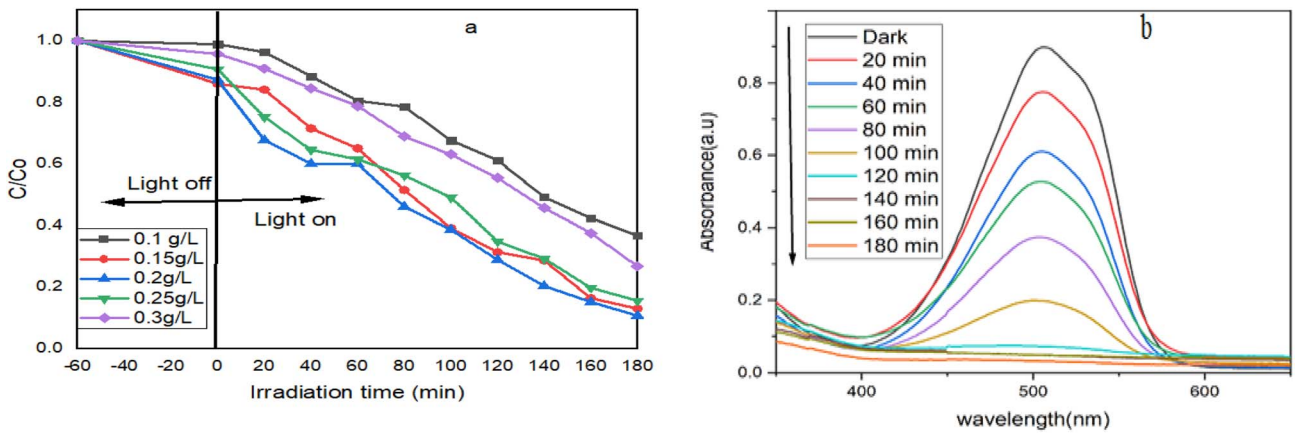

Fig. 8 (a) Effect of catalyst load on the photocatalytic activities of the as-synthesized composite with respect to irradiation time and (b) UV-visible spectra of the MO dye solution irradiated in 20-min intervals using 0.20 g L^{-1} of GUA2, 15 ppm dye concentration and pH 2.

irradiation time obtained by varying the photocatalyst amount is shown in Fig. 8. The observed improvement in MO decolorization efficiency within the range of g-C_3N_4/UiO-66/Ag_2CrO_4 catalyst concentrations from 0.10 to 0.20 g L^{-1} may be caused by more accessible adsorption and catalytically active sites on the g-C_3N_4/UiO-66/Ag_2CrO_4 catalyst surface. However, an additional rise in catalyst concentration may result in an increase in opacity and a light scattering effect, which would lower its specific activity due to the aggregation of g-C_3N_4/UiO-66/Ag_2CrO_4 (GUA2) particles at high dosages. The experimental results showed that as the catalyst load increased from 0.10 to 0.20 g L^{-1}, the degradation of MO by GUA2 also increased from 81.22% to 89.3%. However, the further increase in the catalyst load from 0.20 to 0.30 g L^{-1} decreased its degradation efficiency of MO from 89.3% to 73.20%, and this was done without the optimization of dye concentration. The amount of photocatalyst increased only up to some point, and further increment in the amount of the catalyst decreased the degradation efficiency due to the decreased light penetration caused by the shielding effect of the overdosed suspended particles of the GUA2 photocatalyst. The mass of the catalyst directly correlates with the first rate of reaction. Nevertheless, the response rate levels out and becomes independent of mass over a specific mass.[30] As the dosage of photo-catalyst increased, the total surface area (active sites) available for the photocatalytic reaction likewise appeared to have increased, contributing to the increase in MO efficiency. However, at the same time, as the suspension's turbidity increased, visible light penetration reduced due to an increased scattering effect, which lowered the suspension's photo-initiated volume. When the concentration of the solid particles is higher, the tendency of particle–particle interaction (agglomeration) increases, which reduces the surface area available for light absorption and decreases the photocatalytic degradation rate.[31] In addition to this, a decrease in photocatalytic rate was due to an unfavorable light scattering, and the reduction of light penetration into the solution was observed with excess photocatalyst loading.

3.7.3. Initial MO dye concentration. The initial concentration of the organic pollutant (MO) was another significant experimental element that influenced photocatalytic degradation. Using g-C_3N_4/UiO-66/Ag_2CrO_4, the effect of the initial concentration of MO solution on the degrading effect under visible irradiation was investigated by increasing the concentrations from 5 to 20 ppm at a fixed photocatalyst load (0.2 g L^{-1}) and pH 2. As the dye concentration increased from 5 to 10 ppm, the initial rate of MO degradation by GUA_2 increased, as seen in Fig. 9. When the dye concentration was 5 ppm, 82.1% of the dye was eliminated after 180 minutes; when the concentration was raised to 10 ppm of MO, the degradation increased to 97.00%, as illustrated in Fig. 9. However, as the dye concentration increased from 10, 15, and 20 ppm, GUA2's dye degradation efficiency dropped from 97.00%, 70.70%, and 60.9%. As the concentration of dye increased from 5 to 20 ppm, the corresponding degradation rate constant (K) value of dye degradation likewise increased from 0.0096 min^{-1} to 0.0195 min^{-1} and declined from 0.0195 min^{-1}, 0.0068 min^{-1}, and 0.0052 min^{-1}, respectively, with irradiation duration. Because there were fewer active sites accessible relative to the amount of MO molecules present at high concentrations, MO degradation decreased as concentration increased. This reduced the photodegradation effectiveness by preventing the light's photons from interacting with the system.[32]

3.7.4. Effect of scavengers. The results showed that 97.00% of MO was converted photo-catalytically without the need for

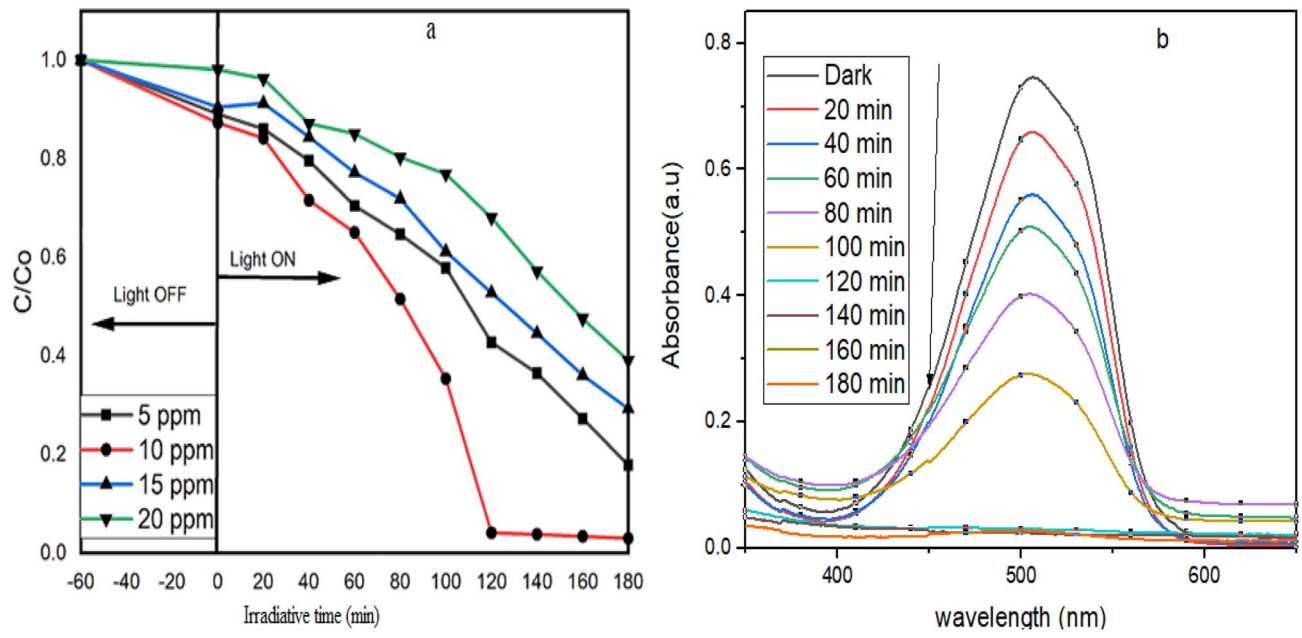

Fig. 9 (a) Effect of initial dye concentration on the photocatalytic activities of the as-synthesized nanocomposites with respect to irradiation time using 10 ppm dye concentration and at pH 2 and (b) UV-visible spectra of the MO dye solution irradiated in 20-min intervals at pH 2 using 10 ppm dye concentration and 0.20 g per L GUA2 catalyst load.

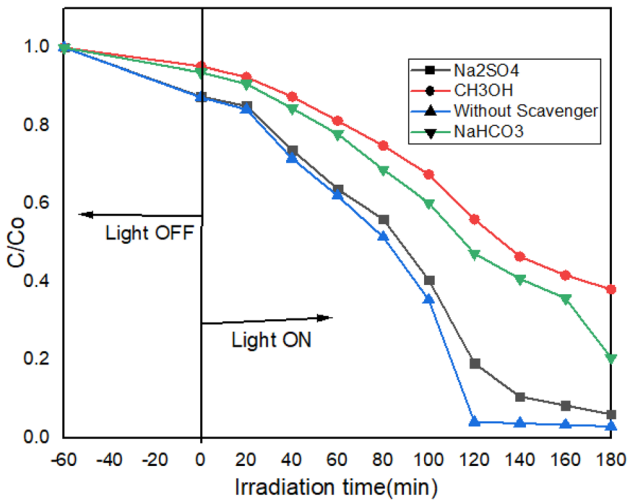

Fig. 10 Photocatalytic degradation of MO over g-C_3N_4/UiO-66/Ag_2CrO_4 (GUA2) samples under visible-light irradiation at optimized parameters with the addition of different scavengers, CH_3OH, $NaHCO_3$, and Na_2SO_4, and without a scavenger.

a scavenger. However, the photocatalytic degradation of MO dropped to 93.90% when Na_2SO_4 (*O_2) was added, while the photocatalytic conversion of dye became 61.90% and 79.40%, respectively, when CH_3OH/H_2O (*OH) and $NaHCO_3$ (h^+) were applied. The addition of Na_2SO_4 slowed the dye's photodegradation, whereas the addition of $NaHCO_3$ or CH_3OH/H_2O significantly slowed it down. This suggested that the hole (h^+) and hydroxide radicals (*OH) were the primary drivers of dye degradation, with superoxide radicals playing a minor role (Fig. 10).

3.8. Photocatalytic stability of the as-synthesized photocatalyst (GUA2)

Fig. 11 illustrates that after 120 minutes of radiation, 97.00% of the dye was destroyed in the first cycle. According to Fig. 11, the dye was degraded by 94.60%, 90.20%, and 87.90% in the first, second, and third cycles, respectively, with rate constants (K) of 0.0162 min^{-1}, 0.0129 min^{-1}, and 0.0127 min^{-1}. The agglomeration and settling of the dye around GUA2 particles after each cycle of photocatalytic degradation may be the cause of the observed drop in the degradation rate. This is due to the fact that the photocatalyst's surface becomes unavailable for dye adsorption and, as a result, photon absorption each time it is reused, which reduces the catalytic reaction's effectiveness.[33,34] A photocatalyst loss during recycling may also be expected, which eventually impacts catalytic activity after every cycle. This decreases the rate at which the as-synthesized photocatalyst degrades. This can be because some of the catalyst is lost during the cycling reaction or the catalyst's absorbance capacity weakens. The result demonstrated that the g-C_3N_4/UiO-66/Ag_2CrO_4 ternary nanocomposite showed excellent photocatalytic performance and good stability after three repetitive cycles in 180 min.

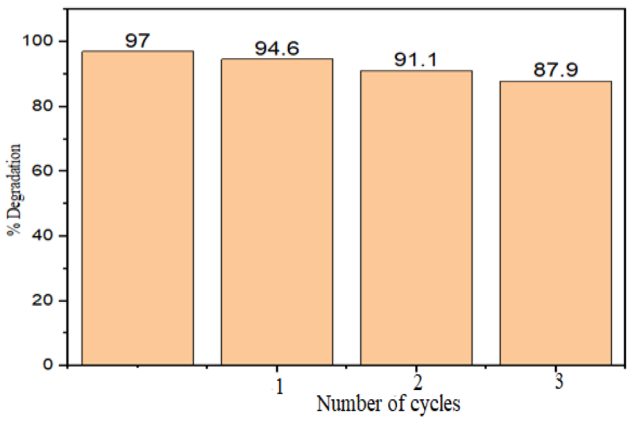

Fig. 11 Reusability test for the GUA2 (g-C_3N_4/UiO-66/Ag_2CrO_4) photocatalyst under visible-light irradiation for three consecutive cycles.

3.9. Real sample treatment under visible-light irradiation

The efficiency of the as-synthesized g-C_3N_4/UiO-66/Ag_2CrO_4 photocatalyst for the degradation of the real sample under visible-light irradiation was studied for 180 min. Fig. 12 showed that the percentage degradation of the model pollutant (MO) aqueous solution and the real sample was found to be 97.00% and 76.20%, with a k value of 0.0195 min^{-1} and 0.0079 min^{-1}, respectively. The outcome showed that, in comparison to that on the optimized model pollutant (MO), the degrading efficiency of GUA2 on the actual sample solution was lower. This could be because the wastewater contained a greater quantity of different sorts of dyes. It is well known that the textile industry uses a variety of anionic and cationic dyes in combination.

In addition, the photodegradation of MO and real sample by this catalyst was evaluated under a solar light (outdoor) system. The photocatalytic efficiency obtained under the outdoor system on MO and real sample degradation was higher (99.6% and 79.01%, respectively) than that given under visible-light

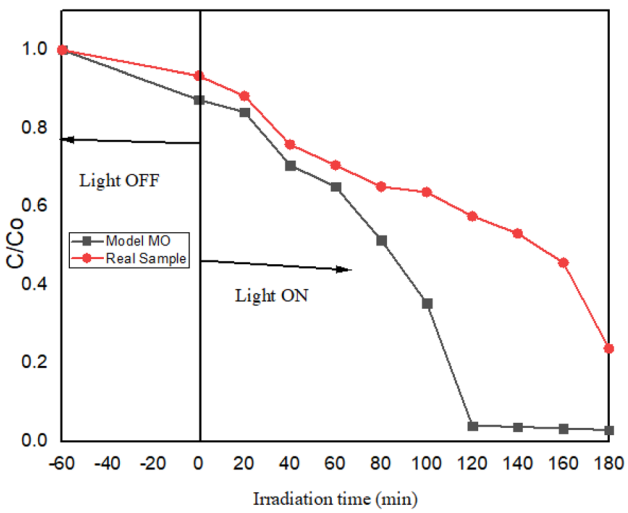

Fig. 12 Photocatalytic degradation of MO and real textile wastewater by the selected photocatalyst (GUA2).

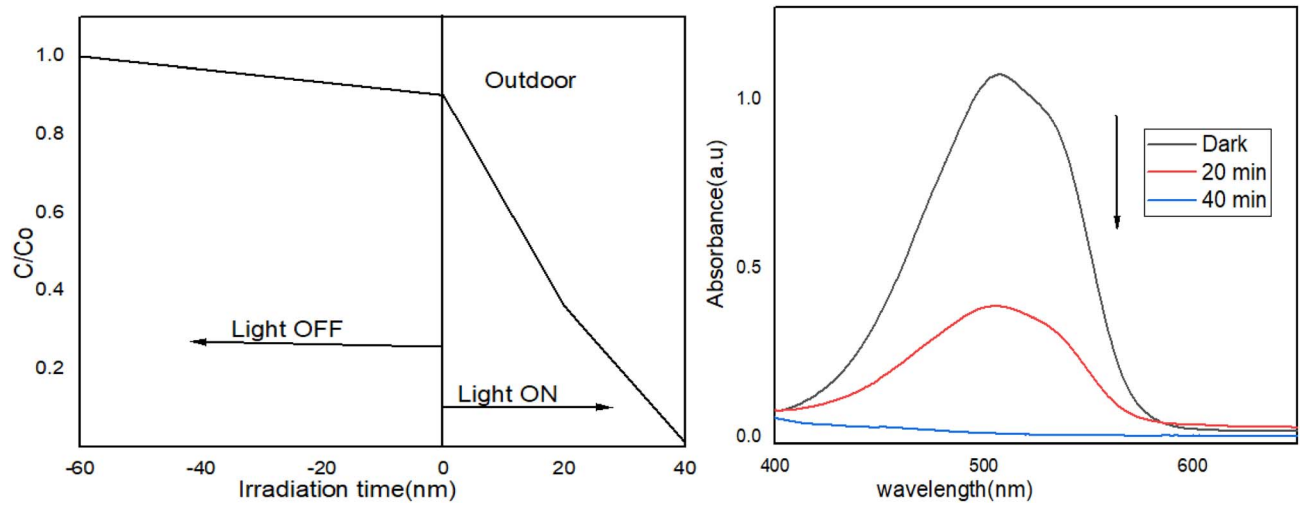

Fig. 13 Photocatalytic activity of the GUA2 composite with respect to irradiation time and UV-vis spectra of the MO dye solution irradiated in 20-min intervals in the outdoor system.

irradiation (indoor system). The higher photoactivity outdoors might be due to the higher intensity of the solar light. According to the result presented in Fig. 13, in the outdoor system, the degradation of MO by GUA2 was completed after 40 min, which indicated that the time taken for the degradation of MO dye was threefold less than that for the degradation of MO in the visible-light irradiation (indoor system).

3.10. Photocatalytic mechanism of the g-C_3N_4/UiO-66/Ag_2CrO_4 (GUA2) catalyst

An examination of the conduction and valence band edges of the constituent materials clarified the photocatalytic mechanism of the produced GUA2 catalyst. When photon energy equal to or greater than the composite's bandgap is absorbed, the photocatalytic process begins, causing the visible active components (A and G) to photogenerate electrons and holes. Silver (Ag_2) nanoparticles that were created *in situ* during the reaction greatly increased the photocatalytic activity by boosting the surface resonance effects on the Ag_2CrO_4 and the Zr-BDC framework. Unlike more conventional transfer processes, these Ag_2 nanoparticles enabled an effective electron–hole transfer mechanism that resembled a straight Z-scheme. This has an impact on catalytic activity after every cycle.

To explain the observed photocatalytic activity, the positions of the valence band (VB) and conduction band (CB) edges were estimated using the following equations:

$$E_{VB} = X - E_0 + 0.5E_g, \quad (4)$$

$$E_{CB} = E_{VB} - E_g. \quad (5)$$

The study explored the photocatalytic mechanism of the g-C_3N_4/UiO-66/Ag_2CrO_4 nanocomposite. Here, E_g represents the bandgap energy, and E_{VB} and E_{CB} denote the energies of the valence and conduction bands, respectively. For semiconductors A, G, and U (Zr-BDC), we noted their absolute electronegativity values as 5.86 eV, 4.73 eV and 6.2 eV, respectively.[35,36] We set E_0 at 4.5 eV, which is the energy for free electrons on the hydrogen scale, while the corresponding bandgaps for A, G, and U were 1.90, 2.57, and 3.80 eV. For semiconductor A, the conduction band (CB) and valence band (VB) energies were +0.41 eV and +2.31 eV (*vs.* NHE). This meant that electrons in the CB could not reduce dissolved oxygen into superoxide radicals, as the CB potential was more positive than that of O_2/O_2^* (−0.33 eV *vs.* NHE). Similarly, for G, the CB and VB values were −1.05 eV and +1.51 eV (*vs.* NHE). This indicated that the holes generated in G's VB could not react with water to create hydroxyl radicals due to their insufficient potential. For U (Zr-BDC), the CB and VB energies were −0.20 eV and +3.60 eV, respectively.

By considering the band positions of each component, we proposed a synergistic mechanism to explain the photocatalytic process. Both G and A generated electrons from their VB to CB when exposed to light, creating charge carriers. However, the usual charge transfer was hindered by the differences in flat band potentials among the components. T suggested an S-scheme mechanism, where silver (Ag_0) nanoparticles played a key role in facilitating the efficient transfer of these photogenerated charge carriers.

In this S-scheme setup, the photogenerated electrons from the CB of G and A moved through the Ag_0 nanoparticles, thanks to their low Fermi energy level, reaching the lowest unoccupied molecular orbital (LUMO) of the terephthalate in the Zr-BDC structure. This electron transfer led to movement towards the Zr-oxo cluster *via* a ligand-to-metal charge transfer (LMCT), which reduced Zr^{4+} to Zr^{3+}. As a result, the electrons injected into the Zr-BDC reacted with O_2 molecules on its surface, reducing superoxide anions and ultimately breaking down methyl orange (MO) into water and carbon dioxide. This process was driven by the high intervalence potential of the Zr^{3+}/Zr^{4+} redox couple. Meanwhile, the electrons remained in the CB of A, contributing to the overall photocatalytic action.

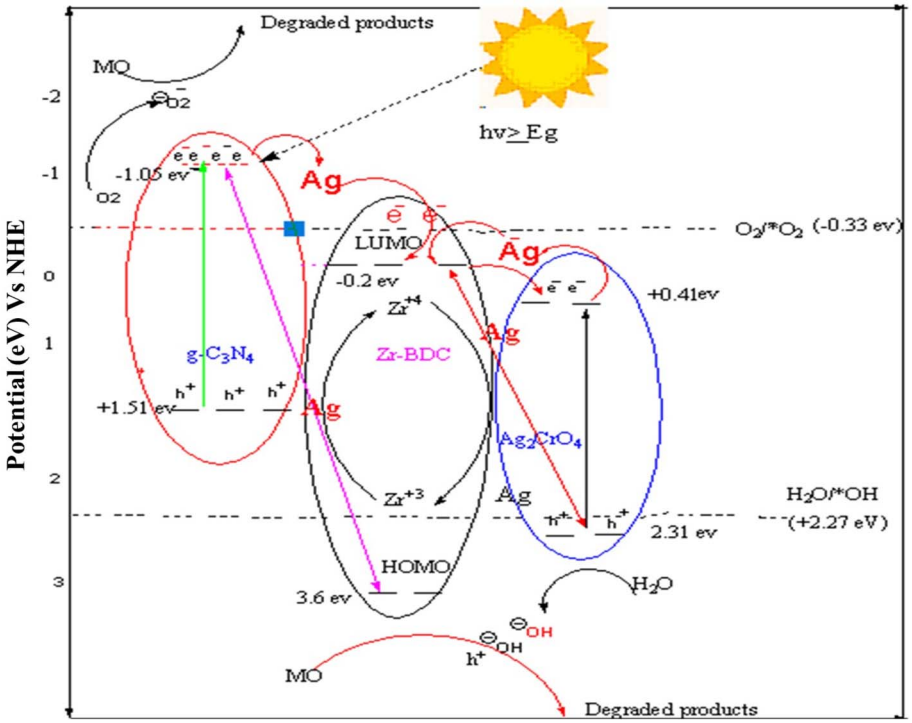

Fig. 14 Schematic of the mechanism of the photodegradation of the organic contaminant (MO) using g-C_3N_4/UiO-66/Ag_2CrO_4 as a photocatalyst under visible-light irradiation.

The oxidation of MO under visible light required the holes and hydroxyl radicals produced by A and Zr-BDC. Furthermore, the duration of electron–hole pair recombination was greatly extended by the Ag_2 nanoparticles. Ultimately, the holes and electrons formed by the VBs and CBs of A and U were transferred and recombined with the Ag_2 nanoparticles, assisting in the production of hydroxyl radicals from the photogenerated holes. The outcomes of our scavenger investigations were in line with this suggested mechanism (Fig. 14).

4. Conclusions

In this study, a novel g-C_3N_4/UiO-66/Ag_2CrO_4 (GUA2) ternary nanocomposite with high photocatalytic activity and stability was successfully synthesized *via* the precipitation method and studied systematically for the photodegradation of MO under visible-light irradiation (indoor) and in outdoor systems. The bandgap energy, crystal structure, morphology, optical properties, and functional groups of the as-synthesized photocatalysts were characterized using UV/visible, XRD, SEM, PL, and FTIR instruments, respectively. After 120 min of visible-light irradiation, about 97.0% of MO was degraded by the GUA2 composite, which was better than those of the other as-synthesized materials. The result showed that after 40 min of solar-light irradiation (outdoor system), about 99.6% of methyl orange was degraded by the GUA2 composite. This indicated that the time taken for the degradation of MO by the GUA2 composite in an outdoor system was three times less than that for an indoor system. Therefore, the g-C_3N_4/UiO-66/Ag_2CrO_4 ternary nanocomposite may be a good option for industrial photocatalytic applications, particularly in the cleaning of the environment and the purification of wastewater that contains organic dyes. However, monitoring relied on dye decolorization only; total organic carbon (TOC) removal and identification of intermediate/by-products were not performed, so the formation of potentially toxic intermediates cannot be ruled out. Future work should include TOC and by-product analyses, tests with real wastewater samples, long-term stability and leaching studies, mechanistic investigations, and scale-up assessments to validate practical applicability and safety.

Conflicts of interest

There are no conflicts of interest.

Data availability

All relevant data are included within the manuscript.

References

1 J. Ding, Z. Yang, C. He, X. Tong, Y. Li, X. Niu and H. Zhang, UiO-66 (Zr) coupled with Bi2MoO6 as photocatalyst for visible-light promoted dye degradation, *J. Colloid Interface Sci.*, 2017, **497**, 126–133.
2 J. Wang, J. Liu, Q. Tong, Y. Lu and X. Yang, High Degradation Activity and Quantity Production of Aluminum- Doped Zinc Oxide Nanocrystals Modified by Nitrogen Atoms, *Ind. Eng. Chem. Res.*, 2014, **53**(6), 2229–2237.

3 M. Alvaro, E. Carbonell, B. Ferrer and F. X. Llabrøs, Semiconductor Behavior of a Metal-Organic Framework (MOF), *Chem.–Eur. J.*, 2007, 5106–5112.
4 J. H. Cavka, S. Jakobsen, U. Olsbye, N. Guillou, C. Lamberti, S. Bordiga and K. P. Lillerud, A new zirconium inorganic building brick forming metal organic frameworks with exceptional stability, *J. Am. Chem. Soc.*, 2008, **130**(42), 13850–13851.
5 H. Wu, Y. S. Chua, V. Krungleviciute, M. Tyagi, P. Chen, T. Yildirim, *et al.*, Unusual and Highly Tunable Missing-Linker Defects in Zirconium Metal–Organic Framework UiO-66 and Their Important Effects on Gas Adsorption, *J. Am. Chem. Soc.*, 2013, **135**(28), 10525–10532.
6 L. Huang and B. Liu, Synthesis of a novel and stable reduced graphene oxide/MOF hybrid nanocomposite and photocatalytic performance for the degradation of dyes, *RSC Adv.*, 2016, **125**, 17873–17879.
7 Y. Wang, Y. Zhang, Z. Jiang, G. Jiang, Z. Zhao, Q. Wu, *et al.*, Controlled fabrication and enhanced visible-light photocatalytic hydrogen production of Au @ CdS/MIL-101 heterostructure, *Appl. Catal., B*, 2016, **185**, 307–314.
8 X. Zhang, Y. Yang, W. Huang, Y. Yang, Y. Wang and C. He, g-C3N4/UiO-66 nanohybrids with enhanced photocatalytic activities for the oxidation of dye under visible light irradiation, *Mater. Res. Bull.*, 2018, **99**, 349–358, DOI: 10.1016/j.materresbull.2017.11.028.
9 A. H. Alia, I. Diazb and A. A. Tsegayec, Polyaniline Supported g-C3N4/CeO2 Fluorescent Chemosensor for Selected Heavy Metal and Nitrate Ions Determination, *Acta Chem. Iasi*, 2022, **88**, 45–88.
10 A. Hadush, T. Kebede, A. M. Taddesse, N. R. Habib and M. Sánchez-Sánchez, Enhanced photocatalytic performance of rGO/UiO-66(Zr)/Ag3PO4 composite for degradation of methyl orange (MO) under visible light irradiation, *Opt. Mater.*, 2024, **155**, 115901.
11 J. K. Ebrahim, Cu2O/UiO-66/Ag2CO3 Nanostructured Material as Nonenzymatic Electrochemical Sensor for the Determination of Glucose, Master's thesis, Haramaya University, Ethiopia, 2017.
12 H. Zeng, Z. Yu, L. Shao, X. Li, M. Zhu, Y. Liu, X. Feng and X. Zhu, Ag2CO3@UiO-66-NH2 embedding graphene oxide sheets photocatalytic membrane for enhancing the removal performance of Cr(VI) and dyes based on filtration, *Desalination*, 2020, **491**, 114558.
13 C. G. Silva, I. Luz, F. X. Llabrøs and A. Corma, Water Stable Zr – Benzenedicarboxylate Metal – Organic Frameworks as Photocatalysts for Hydrogen Generation, *Chem.–Eur. J.*, 2010, **16**, 11133–11138.
14 Z. Sha, H. Sze On Chan and J. Wu, Ag2CO3/UiO-66(Zr) composite with enhanced visible- ight promoted photocatalytic activity for dye degradation, *J. Hazard. Mater.*, 2015, **299**, 132–140, DOI: 10.1016/j.jhazmat.2015.06.016.
15 S. Panumati, K. Chudecha, P. Vankhaew, V. Choolert, L. Chuenchom, W. Innajitara, *et al.*, Adsorption of phenol from diluted aqueous solutions by activated carbons obtained from bagasse , oil palm shell and pericarp of rubber fruit, *Songklanakarin J. Sci. Technol.*, 2008, **30**(2), 185–189.
16 X. Zhao, X. Liu, Z. Zhang, X. Liu and W. Zhang, Hybrid with enhanced photocatalytic activity under visible light irradiation†, *RSC Adv.*, 2016, 92011–92019.
17 S. Kaur and V. Singh, TiO 2 mediated photocatalytic degradation studies of Reactive Red 198 by UV irradiation, *J. Hazard. Mater.*, 2007, **141**, 230–236.
18 V. Gupta, A. R. Gupta and V. Kant, Synthesis, characterization and biomedical application of nanoparticles, *Sci. Int.*, 2013, **1**(5), 167–174.
19 A. C. Dodd, A. J. Mckinley, M. Saunders and T. Tsuzuki, Effect of particle size on the photocatalytic activity of nanoparticulate zinc oxide, *J. Nanopart. Res.*, 2006, **8**, 43–51.
20 Z. Zhang, J. Liu, P. Y. Gu, R. Ji, L. Jin, S. Zhou, J. He, D. Chen, Q. Xu and J. Lu, Preparation of a Bi12O15Cl6@ W18O49@ g-C3N4/PDI heterojunction with dual charge transfer paths and its photocatalytic performance for phenolic pollutants, *Sep. Purif. Technol.*, 2022, 120539.
21 X. Zhang, Y. Yang, W. Huang, Y. Yang, Y. Wang, C. He, N. Liu, M. Wu and L. Tang, g-C3N4/UiO-66 nanohybrids with enhanced photocatalytic activities for the oxidation of dye under visible light irradiation, *Mater. Res. Bull.*, 2018, **99**, 349–358.
22 L. Shi, L. Liang, F. Wang, M. Liu and J. Sun, Ag2CrO4 nanoparticles loaded on two-dimensional large surface area graphite-like carbon nitride sheets: simple synthesis and excellent photocatalytic performance, *Dalton Trans.*, 2016, **45**(13), 5815–5824.
23 Z. Yang, X. Xu, X. Liang, C. Lei, Y. Cui, W. Wu, *et al.*, Construction of heterostructured MIL-125/Ag/g-C 3 N 4 nanocomposite as an efficient bifunctional visible light photocatalyst for the organic oxidation and reduction reactions, *Appl. Catal., B*, 2017, **205**, 42–54, DOI: 10.1016/j.apcatb.2016.12.012.
24 A. H. Ali, I. Diaz, A. A. Tsegaye and A. T. Mengesha, Polyaniline supported g-c3n4/ceo2 fluorescent chemosensor for selected heavy metal and nitrate ions determination, *Acta Chem. Iasi*, 2022, **30**, 45–88.
25 F. Soofivand, F. Mohandes and M. Salavati-niasari, Silver chromate and silver dichromate nanostructures: Sonochemical synthesis , characterization , and photocatalytic properties, *Mater. Res. Bull.*, 2013, **48**(6), 2084–2094, DOI: 10.1016/j.materresbull.2013.02.025.
26 Y. Chiang and C. Lin, Photocatalytic decolorization of methylene blue in aqueous solutions using coupled ZnO/SnO 2 photocatalysts, *Powder Technol.*, 2013, **246**, 137–143, DOI: 10.1016/j.powtec.2013.04.033.
27 H. Reza, M. Roushani and M. Shamsipur, Development of a highly selective voltammetric sensor for nanomolar detection of mercury ions using glassy carbon electrode modified with a novel ion imprinted polymeric nanobeads and multi-wall carbon nanotubes, *J. Electroanal. Chem.*, 2013, **693**, 16–22.
28 P. Tatar, N. Kiraz, E. Arpac and H. Sayılkan, Photocatalytic performance of Sn-doped TiO2 nanostructured mono and double layer thin films for Malachite Green dye

degradation under UV and vis-lights, *J. Hazard. Mater.*, 2007, **144**, 140–146.

29 J. M. Yassin, A. M. Taddesse and M. Sancvhez-Sanchez, Sustainable synthesis of a new semiamorphous Ti-BDC MOF material and the photocatalytic performance of its ternary composites with Ag3PO4 and g-C3N4, *Appl. Surf. Sci.*, 2022, **578**, 151996.

30 M. V. Shankar, S. Anandan, N. Venkatachalam, B. Arabindoo and V. Murugesan, Novel thin-film reactor for photocatalytic degradation of pesticides in an aqueous solution, *J. Chem. Technol. Biotechnol.*, 2004, **79**(11), 1279–1285.

31 R. Das, Application Photocatalysis for Treatment of Industrial Waste Water—A Short Review, *OALib*, 2014, **1**, 1–17.

32 H. Tedla, I. Diaz, T. Kebede and A. M. Taddesse, Synthesis, characterization and photocatalytic activity of zeolite supported ZnO/Fe2O3/MnO2 nanocomposites, *J. Environ. Chem. Eng.*, 2015, **3**(3), 1586–1591, DOI: 10.1016/j.jece.2015.05.012.

33 P. Wang, B. Huang, X. Qin, X. Zhang, Y. Dai, J. Wei and M.-H. Whangbo, Ag@AgCl : A Highly Efficient and Stable Photocatalyst Active under visible light, *Angew. Chem., Int. Ed.*, 2008, **47**, 7931–7933.

34 W. Zhang, C. Hu, W. Zhai, Z. Wang, Y. Sun, F. Chi, *et al.*, Novel Ag3PO4/CeO2 p–n Hierarchical Heterojunction with Enhanced Photocatalytic Performance, *Mat. Res.*, 2016, **19**(3), 673–679.

35 S. Chen, Y. Hu, S. Meng and X. Fu, Study on the separation mechanisms of photogenerated electrons and holes for composite photocatalysts g-C 3 N 4 -WO 3, *Appl. Catal., B*, 2014, **150–151**, 564–573, DOI: 10.1016/j.apcatb.2013.12.053.

36 J. Zhang, W. Yu, J. Liu and B. Liu, Illustration of high-active Ag2CrO4 photocatalyst from the first-principle calculation of electronic structures and carrier effective mass, *Appl. Surf. Sci.*, 2015, 6–11, DOI: 10.1016/j.apsusc.2015.08.084.